CrossMark

ORIGINAL PAPER

The most frequent interfaces in olivine aggregates: the GBCD and its importance for grain boundary related processes

Katharina Marquardt[1] · Gregory S. Rohrer[2] · Luiz Morales[3] · Erik Rybacki[3] · Hauke Marquardt[1] · Brian Lin[2]

Abstract Rocks consist of crystal grains separated by grain boundaries that impact the bulk rock properties. Recent studies on metals and ceramics showed that the grain boundary plane orientation is more significant for grain boundary properties than other characteristics such as the sigma value or disorientation (in the Earth's science community more frequently termed misorientation). We determined the grain boundary character distribution (GBCD) of synthetic and natural polycrystalline olivine, the most abundant mineral of Earth's upper mantle. We show that grain boundaries of olivine preferentially contain low index planes, in agreement with recent findings on other oxides (e.g. MgO, TiO_2, Al_2O_3 etc.). Furthermore, we find evidence for a preferred orientation relationship of 90° disorientations about the [001] direction forming tilt and twist grain boundaries, as well as a preference for the 60° disorientation about the [100] axis. Our data indicate that the GBCD, which is an intrinsic property of any mineral aggregate, is fundamental for understanding and predicting grain boundary related processes.

Keywords Olivine · Grain boundaries · Grain boundary plane · GBCD · GBPD · TEM · EBSD · Grain · Boundary processes · Grain boundary energy · Interfacial energy

Communicated by Timothy L. Grove.

✉ Katharina Marquardt
katharina.marquardt@uni-bayreuth.de

1 Bayerisches Geoinstitut, Universität Bayreuth, Bayreuth, Germany

2 Carnegie Mellon University, Pittsburgh, PA, USA

3 Deutsches GeoForschungsZentrum Potsdam, Potsdam, Germany

Introduction

Olivine is the most important phase in the Earth's upper mantle, where the bulk rock composition varies on average from lherzolitic to harzburgitic, where the olivine fractions are normally >60 %. Olivine is of major importance for Earth's mantle dynamics and the presence of grain boundaries in olivine and their type might partially be responsible for attenuation phenomena as well as thermal and diffusion anisotropy observed in seismic studies (Sobolev et al. 1996; Hammond and Humphreys 2000; Toomey et al. 2002; Villagomez et al. 2014). Furthermore, the importance of anisotropic grain boundary properties for fluid (including melt) percolation has been a field of controversial debate (Faul 2001; Hiraga et al. 2007; Gardés et al. 2012; Dai et al. 2013; Ghanbarzadeh et al. 2014). In this contribution, we focus on the full characterization of all 5 independent grain boundary parameters for both natural and synthetic polycrystalline olivine samples, with the goal to determine the anisotropy of olivine grain boundaries in olivine dominated rocks.

In the introduction, we first highlight the general importance of grain boundaries and summarize the current state of knowledge on olivine grain boundaries followed by an overview on melt distribution on the grain scale as this is a topic where many studies have been performed.

This is followed by an overview on how grain boundary properties are studied.

The geometry of grain boundaries and how they can be characterized in their full parameter space is introduced in the third paragraph of the introduction, we aim to give the reader an insight into the most commonly used concepts to differentiate different grain boundary types.

Finally, the last part introduces the methods to measure the grain boundary character distribution.

Grain boundaries in olivine bearing rocks

Grain boundaries are interfaces between two grains of the same mineral. They represent two dimensional defects of the crystal structure that affect a number of physical and chemical properties, such as diffusion, reaction rates, electrical conductivity, or segregation. Examples showing that element diffusion rates along dislocations and grain boundaries are orders of magnitude faster compared to transport rates through the crystal lattice are given by various authors (Atkinson and Taylor 1979; Kaur et al. 1995; Hayden and Watson 2008; Keller et al. 2010; Marquardt et al. 2011). In addition, grain boundaries and individual dislocations can evolve to potential fluid pathways in various rocks [e.g. Worden et al. 1990; Fitz Gerald et al. 2006; Hartmann et al. 2008; Kruhl et al. 2013). Another geologically important process is the capability of grain boundaries to store incompatible elements by grain boundary segregation (Hiraga and Kohlstedt 2007). In polycrystalline aggregates it is not resolved if specific grain boundaries are controlling the grain boundary network, as would be the case if the polycrystal would be made of isomorphic single crystals, each displaying their equilibrium crystal shape (habit). The equilibrium habit as described in standard text books (Tröger 1967; Deer et al. 1992) has been observed on large single crystals usually grown in fluid. In this case, the surface energy controlling the habit is different from a polycrystal where grain–grain contact dominates the surface (or interface) energy.

Grain boundary networks in olivine aggregates have previously been studied with either a focus on deformation and related development of crystallographic preferred orientation (CPO) (e.g. Tommasi et al. 2008, 2009; Vauchez et al. 2012) or with a focus on partially molten rocks (Hirth and Kohlstedt 1995; Wirth 1996; Cmíral et al. 1998; Faul and Fitz Gerald 1999; Faul et al. 2004; Jackson 2004; Tommasi et al. 2008). The latter studies generally aim at characterizing the grain boundary and melt network through the characterization of wetting behavior of melt on the interfaces. The challenge of characterizing grain boundary networks is a result of the large number of physically distinct grain boundaries arising from the fact that any grain boundary has a minimum of five degrees of freedom (see paragraph on grain boundary geometry below). Most observations are time consuming and hence the number of measurements is limited; statistically significant conclusions about grain boundary characteristics where difficult if not impossible to reach. Garapic et al. (2013) characterized the melt network in olivine aggregates at relatively high resolution in two and three dimensions and compared the melt distribution at different melt volume fractions that indirectly affects properties through the contiguity (Takei 1998). Walte et al. (2003, 2005) performed an in situ study on rock analogues. They found that wetted grain boundaries can arise during normal static grain growth as a result of dynamic events, such as the disappearance of individual grains during growth. However, the surface energy anisotropy of their system was estimated to be negligible (Walte et al. 2003), which may result in different behavior during growth compared to anisotropic systems. Their observations of disequilibrium features resulting from grain growth indicate a relatively continuous porosity–permeability relation, similar to the empirical function (traditional) of Wark and Watson (1998). These results give new input into the discussion of the threshold versus traditional permeability model with the threshold model introduced by Faul in 2001 and described in the next paragraph. Faul and Fitz Gerald (1999) observed that grain disorientations between wetted and dry grain boundaries in a melt containing sample differ. The authors demonstrate that grain boundaries with 60° disorientation about [100] have a higher probability of being melt-free, whereas the interfaces between grains of all other disorientations are equally likely of being wetted or dry. They concluded that the wetting behavior is related to the grain boundary energy and thus grain boundary frequency.

Melt distribution on the grain scale is governed by surface energy minimization, a process potentially related to seismic attenuation, energy dissipation, and reduced strength during deformation (e.g. Suzuki 1987; Hirth and Kohlstedt 1995; Wirth 1996; Cmíral et al. 1998; Faul and Fitz Gerald 1999; Hiraga et al. 2003; Faul et al. 2004; Jackson 2004). The prevailing approximation in dynamic melt segregation, retention and extraction models that aim at describing internal grain boundary networks is isotropy of the surface energy (Bagdassarov et al. 2000; Faul 2001; Wark et al. 2003; Schmeling et al. 2012). Traditional permeability models result in dry grain boundaries and wet triple junctions only, generally these models are geometric models that include wetting properties in form of dihedral angles and are applicable to melts and fluid (Takei 1998; Wark and Watson 1998; e.g. Wark et al. 2003; Takei and Holtzman 2009), with the principle ideas dating back to Smith (1948) and von Bargen and Waff (1986). In contrast, observations show that melt mostly occupies grain boundaries in partially molten lherzolites, which resulted in the suggestion of a unique "threshold" permeability relation for upper mantle melts, where permeability shows a sudden jump when grain boundaries start to wet (Faul 2001). Recently, the first models have been developed that account for grain boundary anisotropy (Becker et al. 2008; Ghanbarzadeh et al. 2014), however without experimental calibration.

Studies on grain boundary properties

The study of grain boundary properties can be divided into two broad categories: (a) studies on individual grain

boundaries (e.g. bicrystal studies; Pond and Vlachavas 1983; Peters and Reimanis 2003; Campbell et al. 2004; Marquardt et al. 2011) and (b) studies averaging over many grain boundaries (e.g. polycrystal studies Farver et al. 1994; Yund 1997; Farver and Yund 2000; Milke et al. 2001; Dai et al. 2008; Marquardt 2011).

The bicrystal approach has the advantage that structure of a specific grain boundary can directly be related to specific properties. To investigate trends of such relations various bicrystals have to be synthesized and studied. Generally a main focus of these studies lay on special, e.g. Σ grain boundaries. However, it has been established that most of these so-called "special" interfaces are not particularly common in polycrystals (Saylor et al. 2003b, 2004b; Vonlanthen and Grobety 2008; Rohrer 2011a), a situation referred to as the "Sigma enigma" (Randle 2002).

The polycrystal approach either differentiates between single crystal and grain boundary properties in the most general way, for example by studying diffusion using depth sectioning methods in combination with the Whipple–Le Claire analytical solution (Le Claire 1963; Kaur et al. 1995; Farver and Yund 2000; Schwarz et al. 2002). Otherwise, many studies determined the lattice disorientation of all adjacent crystals to investigate the varying grain boundary

types and their possible influences on grain boundary properties (Lloyd et al. 1997; Fliervoet et al. 1999; Wheeler et al. 2001). However, this description neglects the grain boundary plane orientation. More details on disorientation and grain boundary plane orientation are given in the paragraph on grain boundary geometry.

Grain boundary geometry

The general challenge with characterizing grain boundary networks is a result of the large number of physically distinct grain boundaries arising from the fact that any grain boundary has a minimum of five degrees of freedom (5 parameters, Fig. 1) in orientation space: 3 rotations for the misorientation, and 2 spherical rotations for the grain boundary plane orientation:

The misorientation (Δg) describes the rotations necessary to bring two adjacent crystals frames (g_1 and g_2) into coincidence. The three rotation angles in either the sample or the crystal reference frame are needed for this operation. The disorientation angle describes the misorientation with the smallest possible rotation angle out of all symmetrically equivalent misorientations that fall within the fundamental zone (=the parameter space that results from
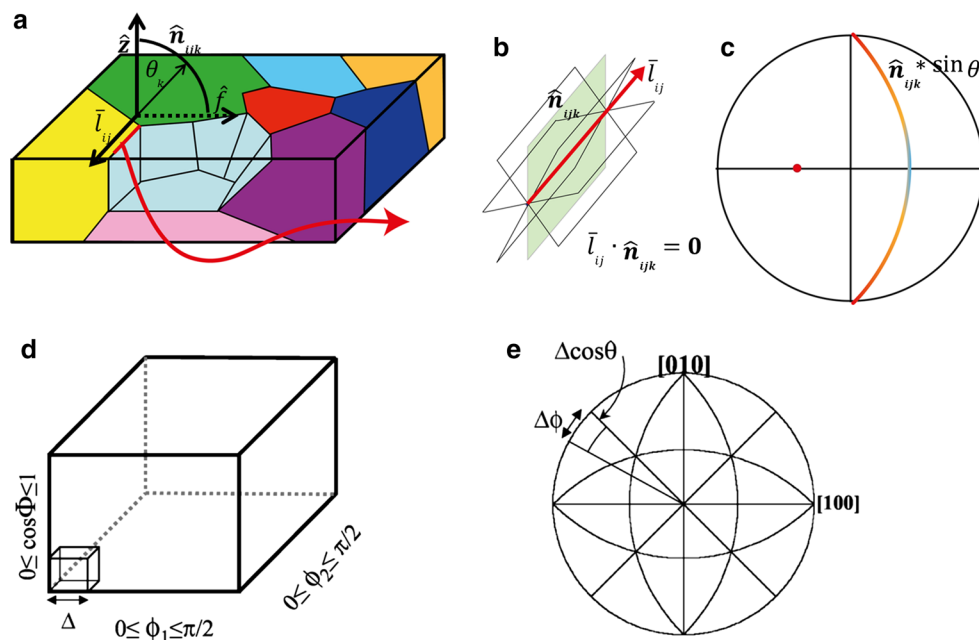

Fig. 1 Stereology, schematic of the principle. **a** Sketch of polycrystalline sample. The definition of the variables in the reference frame of the sample is illustrated. The normal vectors to the possible habit plane, $\hat{n}_{ijk}$, trace a circular arc rotating about the grain boundary trace. **b** Illustration of possible planes corresponding to the trace shown in (**a**). The real habit plane corresponding to the trace is in the zone defined by planes perpendicular to the trace, $\bar{l}_{ij} \cdot \hat{n}_{ijk} = \mathbf{0}$. The probability that the correct plane is in this zone is 1. The probability of sampling planes perpendicular to the observed planar section is

higher than for planes parallel to the surface of the section. The probability variation is shown in (**c**) where poles that plot in the red part of the zone correspond to the traces that are more probable compared to those plotting in the blue range. The parameter space of $\lambda(\Delta g, \mathbf{n})$ is divided into (**d**) three lattice misorientation parameters and (**e**) two boundary plane orientation parameters. The misorientation space has 9^3 cells, each of these cells can be stereographically projected giving the boundary plane normals with 4×9^2 cells (Saylor et al. 2004a, b, c)
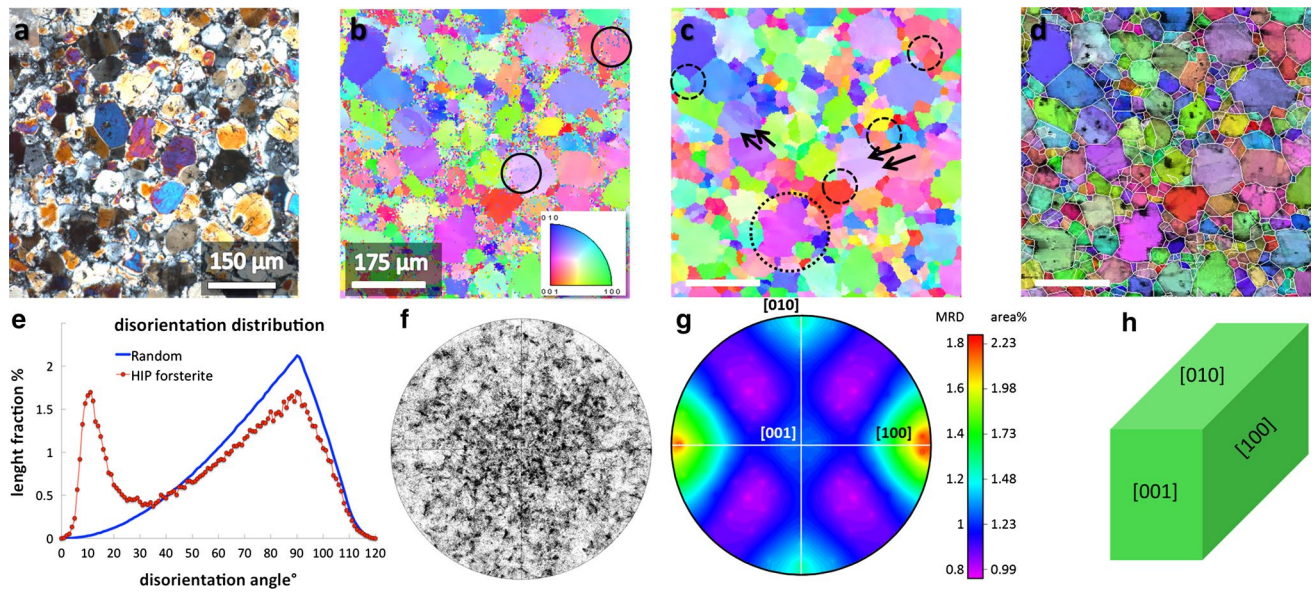
Fig. 2 Hot isostatically pressed forsterite. **a** Micrograph of a thin section, using crossed Nichols. **b–d** EBSD data, depicting the cleanup procedure preceding the export of the reconstructed grain boundary segments. **b** Raw EBSD data, grains where pseudo symmetry of 60° around [100] is present have a speckled appearance, two examples are circled. **c** Data cleaned for pseudo symmetry of 60° around [100], furthermore, grains are dilated to a minimum of 25 pixel total and minimum of 3 pixels in 3 rows, with grain boundaries defined to a minimum of 3° disorientation. Triple junctions with 120° angles are stripe-circled. A large grain with stepped grain boundaries is *dot-circled*. *Arrows* indicate some low angel tilt grain boundaries. **c** The same as **b** but superimposed on the IQ value map. Reconstructed grain boundary segments for grains disoriented by more than 25° are overlaid in *white*. **e** Length fraction of the grain boundary segments versus the disorientation angle of the adjacent crystals, the *blue curve* shows the normal distribution for orthorhombic crystal lattices. **f** Orientation distribution function plotted for each crystals [001] direction. Weak CPO with [001] axis pointing towards the center is displayed. **g** Grain boundary plane distribution. {100} surfaces occur more frequently than {010} and {001} displays a normal distribution, with a relative area ratio of 9:6:5, yielding the simplified crystal shape shown in (**f**)

reduction by the crystal symmetry from the full orientation space available to the fraction of physically distinguishable misorientations. Note that mathematically all available misorientations are distinct. In the orthorhombic crystal system there are 8 symmetry related orientations, thus the size of the full orientation space is in principle reduced by a factor of 8.). In the geological literature misorientation and disorientation are usually not differentiated. In this contribution we use the term disorientation and describe orientations in the Bunge convention with the three Eulerian angles (φ_1, Φ, φ_2) where the first angle refers to a rotation about the z-axis, the second about the x-axis, and the third is another rotation about the z-axis. One can use this convention to either define an orientation in the sample reference frame or the orientation with respect to a neighboring grain. The latter specifies the disorientation, (Δg), that extends to 120° in orthorhombic crystals because disorientations larger than 120° have symmetry related disorientations with a smaller angle. For orthorhombic crystals there are 8 equivalent g, representing the 4 proper and 4 improper symmetry operators for orthorhombic crystal symmetry. We use only the 4 proper operators and imply a center of symmetry that is imposed

by using a diffraction method (EBSD) to obtain our data. The inversion of the grain boundary plane orientation must not be explicitly imposed, but is a result of the method. This reasoning is given by $C_i g$, where C_i ($i = 1$ to 4) are the symmetry operators. The disorientation can be given with respect to the first grain, $\Delta g = C_i g_1 (C_j g_2)^T$, or with respect to the second grain $\Delta g = C_j g_2 (C_i g_1)^T$. This gives a total of $2 \times 4^2 = 32$ equivalent disorientations.

A grain boundary plane is specified by describing its normal in the reference frame of the crystal lattice (**n**) using 2 spherical angles, Θ and ϕ. For each (Δg) the plane normal in the crystal reference frame (**n**) we know the measured planar normal in the sample reference frame $(\mathbf{n}')$ and the non-transposed reference frame; hence, for $\Delta g = C_i g_1 (C_j g_2)^T$, $\mathbf{n} = g C_1 \mathbf{n}'$, and for $\Delta g = C_j g_2 (C_i g_1)^T$, $\mathbf{n} = g C_2 \mathbf{n}'$.

Doing this for the whole data set and plotting the grain boundary plane orientations irrespective of the disorientations of the adjacent crystals yields the grain boundary plane distribution (GBPD). It is stereographically plotted as poles to planes in the crystal reference frame (e.g. Figs. 1c, e, 2g).

The grain boundary character distribution (GBCD) $\lambda(\Delta g, \mathbf{n})$ represents the relative populations of boundaries with different crystallographic characteristics (simply

referred to as character) as a function of the three misorientation angles and the two plane parameters (spherical angles) that sum to the full five macroscopic grain boundary parameters (Saylor et al. 2002, 2003a; Rohrer et al. 2004b). These five angles are parameterized by $\varphi_1, \cos\Phi, \varphi_2, \cos\theta$ and ϕ, so that the domain can be partitioned into equal volume units. Each range of $\pi/2$ is divided into nine discrete cells, and thus the continuous function $\lambda(\Delta g, \boldsymbol{n})$ is approximated by a discrete set of grain boundary types. A visualization of the disorientation domain as a three-dimensional rectangular parallelepiped with indicated parameter ranges is shown in Fig. 1d to illustrate the concept. Each particular disorientation is represented by one individual point in this space, for each disorientation we can plot the distribution of grain boundary plane normals, $\boldsymbol{n}$, on a stereographic projection in the range of $0 \leq \Phi \leq 2\pi$ and $0 \leq \cos\theta \leq 1$, as illustrated in Fig. 1e (Saylor et al. 2004a; Rohrer et al. 2004b). For each of the 9^3 misorientation there are 4×9^2 directions for $\boldsymbol{n}$, and this yields a total of 4×9^5 (236,196) cells in the five-dimensional domain. Of these, 59,049 are crystallographically distinguishable in orthorhombic crystal systems. The distribution of internal grain surfaces, $\lambda(\boldsymbol{n})$, has the same symmetry as the crystal. Thus the GBPD could in principle be displayed in a quarter of the chosen space. However, displaying the GBPD in a full stereographic projection has become common practice as evident from previous work. The full projection is consistent with the GBPD for specific grain boundary disorientations which have reduced symmetries. Projects of the $\lambda(\Delta g, \boldsymbol{n})$ depend on five independent parameters and the symmetry is more complex, therefore the full stereographic net is necessary to display the GBCD and GBPD.

Note that for each grain boundary the plane orientation is given twice, one time for each of the two adjacent crystals. This results in the additional factor of two to the number of symmetrically equivalent grain boundaries in the full domain, thus $2 \times 2 \times 8^2 = 256$ equivalent grain boundaries that could be generated from each observation. However, as we assume a center of symmetry this number is divided by 2 and is partitioned onto the 4 symmetry equivalent subdomains each containing $2 \times 4^2 = 32$ symmetry equivalent grain boundaries.

Geometric concepts to differentiate different grain boundaries have been developed since the middle of the twentieth century. The concept to define a grain boundary included in a bicrystal using these five parameters was first defined by Morawiec (1998), and is well described in his book (Morawiec 2010). The concept is based on the five parameter description of McLean (1957). The grain boundary population is controlled by the grain boundary energy and lower grain boundary energies result in larger grain boundary areas represented by the GBCD. The GBCD is usually displayed linearly in units of multiples of random

distribution (MRD, more details are given in the section "determination of the GBCD") (Saylor et al. 2004c). The GBCD is thus a quantitative description of the amount and type of grain boundaries that are present in a polycrystalline material and, as such, crucial to predict the materials' physical and chemical bulk properties.

The disorientation between adjacent crystals and its relation to dislocation spacings is used to distinguish low angle from high angle grain boundaries. The relation between the spacing of perfect dislocations, d, the disorientation, θ, and the Burgers vector length, $\bar{b}$, was first proposed by Frank (Frank 1951) as: $d = \bar{b}/\theta$. The transition from low- to high angle grain boundaries in most metallic materials occurs between $10°$ and $15°$ disorientation, corresponding to the angle at which individual dislocation cores at the interface cannot any longer be distinguished (Bollmann 1962, 1970; Pond and Bollmann 1979). However, it has been shown that low angle grain boundaries can occur at disorientations as large as $21°$ in olivine (Heinemann et al. 2005) and must be in the range between $22°$ and $32°$ in olivine (Adjaoud et al. 2012). Furthermore, the geometry of the low-angle grain boundary at instances allows the deduction of the active slip system (Friedel 1964; Wenk et al. 1991; Lloyd et al. 1997): the disorientation axis between the sub-grains is perpendicular to the net Burgers vector of the dislocation accommodation the disorientation (Friedel 1964).

High angle grain boundaries are usually divided into general and special grain boundaries, where special grain boundaries are distinguished from general grain boundaries by their special geometric orientations between adjacent crystals (Brandon 1966; Weins et al. 1969). The geometric relation is often described by the coincidence site model (Gleiter and Chalmers 1972; Chadwick and Smith 1976; Sutton and Balluffi 1995). To obtain the coinciding sites, two 3D lattices are super-imposed and rotated/translated until they coincide at lattice sites [see for example Fig. 1 of (Hartmann et al. 2010)] and thereby generate a super periodicity or 'coincidence super lattice', CSL. The $\sum$ value gives the fraction of coinciding lattice points of the two superimposed lattices, n, $\sum = 1/n$ as a characteristic of the CSL. The CSL relations have been generalized for non-cubic materials (King and Singh 1994). The existence of CSL boundaries is a function of the axial ratios. For a $60°$ rotation about the [100] axis in forsterite with a b/c ratio of 1.7 (or c/b = 0.586) the corresponding $\sum$-value is 2. However, if the nearly hexagonal close packed (hcp) oxygen sub-lattice (Poirier 1975) of the (100) planes in forsterite is used to calculate the coincidence site lattice for the axis/angle pair of [100]/$60°$ the $\sum$-value is 3 (Bollmann 1970; Faul and Fitz Gerald 1999). Even if different geometric constraints are used, it appears that the $60°$ disorientation about the [100] axis combines special characteristics. The pseudo-hexagonal closed packed oxygen lattice

in the a-direction in olivine was used to justify the uses of the hexagonal lattice for CSL calculations (Faul and Fitz Gerald 1999). This becomes more valuable when incorporation of Ca in the crystal structure of forsterite results in a change of the unit cell length, especially in the ratio b/c (Grimmer 1989; King and Singh 1994). This results in the formation of pseudo-hexagonal twins of the (011) law, thus 60° disorientation about [100] on (011) planes are formed (Conrad 1935).

We emphasize that the CSL relation does not specify the plane of contact between the two lattices, and the two grains can be joined by different grain boundary planes with different energies. For each specific CSL, high interface coincidences and thus energetic minima only exist for certain grain boundary plane orientations which are likely to occur at the closest packed planes of the corresponding CSL (Rohrer et al. 2004a). Even though well suited to describe special grain boundaries in specific materials, these geometrical descriptions are not sufficient to predict the frequency of general grain boundaries or their physical or chemical properties (Randle 2002). The term general grain boundaries refer to all grain boundaries that cannot easily be described geometrically or by their outstanding properties.

The importance of the grain boundary plane is evident seeing that the area formed by different grain surfaces, or the *grain boundary plane distribution* (*GBPD*), is inversely related to their surface energy (Gleiter and Chalmers 1972; Sutton and Balluffi 1995; Kim and Rohrer 2004; Pang and Wynblatt 2006; Dillon and Rohrer 2009; Rohrer 2011a). This inverse relation of energy and population is well studied for MgO, TiO_2, Al_2O_3 and $SrTiO_3$ (Saylor et al. 2003a, 2004a, b; Pang and Wynblatt 2006). Many other phenomena, such as grain growth and abnormal grain growth are documented and influenced through the GBCD. Unfortunately, studies of the GBPD and GBCD of geological materials are not present in the geological community, with the sole exception of a study on rock salt (Pennock et al. 2009).

Determination of the GBCD using EBSD data

The GBCD of a polycrystalline sample can be obtained from electron backscatter diffraction (EBSD) studies using automated detection of large numbers of grain orientations and grain boundary segments (traces). This concept was fully developed in the field of materials research, mainly for ceramics and metals (Randle 2002; Rohrer 2007, 2011b; Randle et al. 2008), and determination of the GBCD has become a valuable tool in the field of 'grain boundary engineering' (Kim et al. 2005; Watanabe 2011). The GBCD can be measured from 3D EBSD data (e.g. Khorashadizadeh et al. 2011), where EBSD maps are recorded on closely spaced parallel layers, or from 2D EBSD maps analyzed

using stereology (Randle and Davies 2001; Saylor et al. 2004c).

3D EBSD data are obtained from direct 3D geometrical data sets (Saylor et al. 2003a) derived from serial sections of magnesia (MgO, periclase) produced by manual polishing. The automated EBSD acquisition on each planar section taking the section distance into account (Δh) allows for the reconstruction of the three-dimensional grain boundary network and for specifying the disorientation (Δg) and the boundary normal direction (**n**). Li et al. (2009) have investigated the 3D interfacial network of grain boundaries in polycrystalline nickel using a combination of EBSD mapping and focused ion beam for serial sectioning. The details for aligning the sections and skeletonizing the internal grain boundary network is given in (Saylor et al. 2003a). While 3D orientation data are favorable, techniques to obtain 3D data can be challenging and time-consuming. Stereology from 2D EBSD scans provides a feasible alternative.

Stereology on 2D EBSD to obtain the GBCD is based on probability distributions of a grain boundary trace observed in the sample plane; the probability of the surface cutting a perpendicular grain boundary plane is greater than the probability of the surface cutting a parallel grain boundary. This concept is illustrated in Fig. 1a, b, c, which is based on figures from Rohrer et al. (2004b), Saylor and Rohrer (2002). For this analysis, samples with no or minor crystallographic preferred orientation (CPO) are needed to ensure sufficient random distribution (Randle and Davies 2001) and allow for a full characterization of the GBCD (Saylor et al. 2004c; Rohrer 2007, 2011a; Brandon 2010).

The analysis is based on the fact that the frequency with which true habit planes (true surface planes of each crystal) are observed greatly exceeds the frequency with which nonhabit planes are observed (Saylor et al. 2002). If we consider an arbitrary grain boundary plane, in other words one segment of a sphere, intersecting with the observed section (Fig. 1a) its exact plane orientation is not known. However, the true habit plane must belong to the set of planes that include the surface trace, $\bar{l}_{ij}$, (Fig. 1b), and planes perpendicular to the section surface are more frequently intersected, thus resulting in a greater line length, $|l_{ij}|$, than planes inclined to the plane of observation. Mathematically the first condition is given by $\bar{l}_{ij} \cdot \widehat{n}_{ijk} = \mathbf{0}$. The second condition is expressed by using the angle between $\widehat{z}$ and $\widehat{n}_{ijk}$, θ_k to determine the probability of intercepting the plane of observation, which is given by $\sin \theta_k$ (Fig. 1c).

The probability that a given length of line on the perimeter of a random section plane falls on a plane with the orientation **n**, defined in the crystal reference frame, g_i, is:

$$p(n') = \frac{\sum_{i,j,k} g_i n_{ijk} |l_{ij}| \sin \theta_k}{\sum_{i,j,k} |l_{ij}| \sin \theta_k}$$

To determine the crystal shape, knowledge on the relative habit plane areas is needed. The total length of a set of randomly distributed lines intersecting an area is proportional to that area, the ratios of the line lengths associated with each habit plane yields the relative surface area. The areas of all grain boundary segments are summed into the appropriate cells and normalized so that the average value is one. Because the cells have equal volume, the value of $\lambda(\Delta g, \boldsymbol{n})$ in each cell is a multiple of a random distribution (MRD). For any specific grain boundary (e.g. 60° [100](011)), the MRD value is determined by averaging the MRD values of the corresponding 32 symmetry equivalent cells within the domain.

MRD and area percent are related by the discretization of the measurements in the stereographic projection.

Thus, our data are discretized in 10° intervals giving a total of 81 bins. The multiples of random distribution measured per bin yields the area fraction.

$$\frac{\text{MRD}}{\text{No. boxes(bins)}} = \text{area fraction}$$

Fraction area × 100 = %

We extracted 3×10^5 grain boundary line segments, these segments are often a result of summing smaller segments and provide valuable statistics for evaluating the data using the stereological method of Saylor and Rohrer (2002). Grain boundary line segments were evaluated with software developed at Carnegie Mellon University. The scripts were adapted to specifically allow for the evaluation of orthorhombic crystal symmetry, where the domain needed for an adequate description of this lower symmetry compared to all previous GBCD studies had to be enlarged, as described above in the section on the GBCD. Instead of 1/64th of the full range of parameters in the cubic system; for orthorhombic this increases to 1/8th. Consequently instead 2304 general symmetrically equivalent grain boundaries in the full domain of the cubic system, only 256 general symmetrically equivalent grain boundaries are present in the orthorhombic system, always remembering that the amount of distinguishable grain boundaries depends on the angular resolution employed, here 10°.

Furthermore, we wrote a new script to compute the grain surface most likely complementing the grain surface in the adjacent crystal grain forming the mutual interface. In a polycrystalline aggregate the grain boundary plane of one crystal (or the surface of one crystal) defined in its own crystal reference frame is joined by a surface plane in the adjacent crystal, complementing the first crystals surface. We call this the complementing grain boundary plane. It is described in its respective crystal reference frame (see section "grain boundary plane" for more detail). We calculate its statistical likely hood from the grain boundary line segments observed. To find the grain boundary planes most likely complementing a specific grain surface [for example the (100)] we simplify the statistical evaluation previously described and directly assume that any grain boundary that has a trace consistent with a (100) plane actually is a (100) plane. The orientation of the complementary plane in the second crystal is then computed from the knowledge of the grain disorientation. This procedure overestimates the real complementing grain boundary plane distribution, because not all of the traces consistent with (100) actually have that orientation. However, because the GBCD previously calculated indicates that this is the most common plane, the distribution of complements should give a maximum at the true complement. This hypothesis was confirmed by computing the complement distribution in materials with a high population of symmetric twins, where the complement is known with certainty. In all cases, the complement distribution showed a maximum at the expected orientation.

The here-presented GBCDs of natural and synthetic olivine aggregates show an anisotropic area distribution. This is the first study of the GBCD in olivine and the first GBCD for orthorhombic materials in general. From our data we will address the following questions of (1) what are the most common grain boundaries, (2) how relevant are the specific grain boundaries that have been previously investigated (Heinemann et al. 2005; Adjaoud et al. 2012; Ghosh and Karki 2014; Cordier et al. 2014), and (3) how to represent the distribution of grain boundaries in a polycrystalline aggregate?

Samples and methods

Samples

In this paper we investigated two different samples. To characterize the GBCD we characterized a hot isostatically pressed (HIP) forsterite sample with minor CPO (Fig. 2f). This sample was constituted from oxide powder (SiO_2 and MgO) grown forsterite that was crushed and used for the final synthesis in an iron jacket at a temperature of 1200 °C, pressure of 300 MPa for 7 h in a Paterson gas medium triaxial apparatus operating at the German Research Centre for Geosciences (GFZ Potsdam). After the HIP procedure, the sample had a broad unimodal average grain size of 60 μm. As a natural example, we investigated a lherzolite mantle xenolith collected from a volcanic plug in the Auckland island collected by J. Scott [University of Otago—sample AMED-3 in Scott et al. (2014)]. The sample has a mean grain size of 3 mm for the olivine grains, which we accommodate by choosing a larger spacing between individual EBSD measurement spots. The Mg# of these olivines is between 89.7 and 90.3.

Electron backscatter diffraction (EBSD)

For the EBSD measurements, the studied samples were chemi-mechanically polished for 2 h using an alkaline solution of colloidal silica in a soft substrate. The crystallographic orientation measurements were carried out on either coated samples via the automated indexation of EBSD patterns in a scanning electron microscope in low-vacuum mode or on uncoated samples at high vacuum mode. Most of the EBSD analyses were conducted using a FEI Quanta 3D FEG dual beam machine equipped with an EDAX-TSL Digiview IV EBSD detector and the TSL software OIM 5.31 operated at the GFZ Potsdam. For the EBSD crystallographic mapping we have used the following parameters: accelerating voltage of 20 kV, beam current of 8 nA and working distance of 15 mm. For the HIP sample we have used a step size of 5 μm, whereas for the mantle xenolith the step size was 30 μm as the grain sizes were larger. All olivine crystals were mapped using an improved indexation file employing space group Pbnm, and lattice constants $a = 4.762$ Å, $b = 10.225$ Å and $c = 5.994$ Å.

For the analyses of the EBSD maps we used the EDAX® (TSL) OIM software. Grains were defined with a minimum disorientation of 3°, and this fixes the lower limit for the smallest grain boundary disorientation. EBSD data measured on a cubic grid were converted to hexagonal grid. The quality of the indexing of the Kikuchi-patterns is expressed as confidence index (CI) ranging from 0 to 1, where values above 0.2 are sufficient for correct indexing. Our CI values were generally higher than 0.2. We used the following clean-up procedures to remove unindexed and misindexed pixels: As a first step we corrected for pseudo-symmetry. Wrong indexing may occur due to the hexagonal pseudo-symmetry of olivine, where Kikuchi patterns of neighboring measurements are indexed differently resulting in pixels disorientated by 60° about [100], as two solutions fit similarly well to the Kikuchi-pattern and this ambiguity will result in low CI values. This can directly be seen in the EBSD maps where grains of such an orientation look speckled, with two colors corresponding to the two distinct orientations (examples are circled in the raw data displayed in Fig. 2b). This pseudo symmetric misindexing can easily be recognized when highlighting the respective grain boundary traces superimposed on a IQ image, if the grain boundary traces occur on actual grain boundaries, identified by lower IQ values, than they are real grain boundaries. If the traces are in the interior of grains they can be discarded as they result from the poor indexing algorithm (cleaned data are shown in Fig. 2c and superimposed on an IQ image in Fig. 2d).

Furthermore, we dilated grains to absorb points not belonging to any grain (defined as a minimum of 2 neighboring points with the same orientation within 3°) which are frequent observations along grain boundaries where two Kikuchipattern overlap. For those at boundaries, the isolated point becomes part of the grain that surrounds the majority of the point; if two grains surround the individual points equally, the point becomes part of the grain with the highest average CI. The absorbed point takes orientation and CI of the neighboring grain with highest CI. Dilatation was set to result in a minimum of 3 rows of a minimum of 3 pixels each, which did not affect the average grain size determined before and after this procedure. Note, that the grains considered for further analyses were chosen to have a minimum size of 25 pixels over at least 3 rows.

The grain boundary traces are reconstructed into segments. Triple junctions are identified and a straight line is drawn between them. The segments are dissected into shorter segments until the tolerance between the reconstructed line the actual grain boundary is less than twice the step size used for mapping, a schematic explanation is given in Fig. 2 in Pennock et al. (2009). In Fig. 2d only segments tracing grain boundaries formed by disorientations of the grains higher than 25° are plotted.

Subsequently the exported grain boundary line segments were evaluated following the description in the introduction using the scripts developed at the CMU, Pittsburgh.

## Transmission electron microscopy (TEM)

Electron transparent foils were prepared at the GFZ Potsdam using a FEI FIB200. Foil dimensions are 12×10 μm^2 with a thickness of about 150 nm. The foil was recovered using the ex situ-liftout technique (Wirth 2004).

Transmission electron microscopic (TEM) investigations were performed with a FEI Titan 80–200 microscope at BGI Bayreuth, using conventional TEM, high resolution (HR)-TEM as well as scanning (S)-TEM modes. The microscope was operated at an acceleration voltage of 200 kV with an electron beam generated by an extreme brightness field emission gun (X-FEG) Schottky electron source. The TEM is equipped with a post-column Gatan imaging filter (GIF Quantum®SE). In STEM mode, the high angle annular dark field (HAADF) detector and/or the bright or dark field (BF/DF) detectors were used to acquire the signal. For energy dispersive X-ray (EDX) measurements we used the windowless Super X-EDS detector with 4 SDDs.

Results

Sample 1 The hot isostatically pressed forsterite (Fig. 2a) shows a microstructure with widely varying grain sizes (mean 60 μm) and triple junctions are dominated by 120°

Fig. 3 Sample 1 (HIP) observation on the nm-scale. **a** Scanning transmission electron micrograph of two forsterite grains in contact. The *left* grain is close to zone axis orientation and includes two low-angle grain boundaries that are in contact to a large-angle grain boundary. At the triple junction and along the boundary precipitates are observed, see enlargement (**c**). **b** At the triple junction EDS data indicate an elevated amount of Al (*blue spectra*) with respect to the crystal interior (*green spectra*)
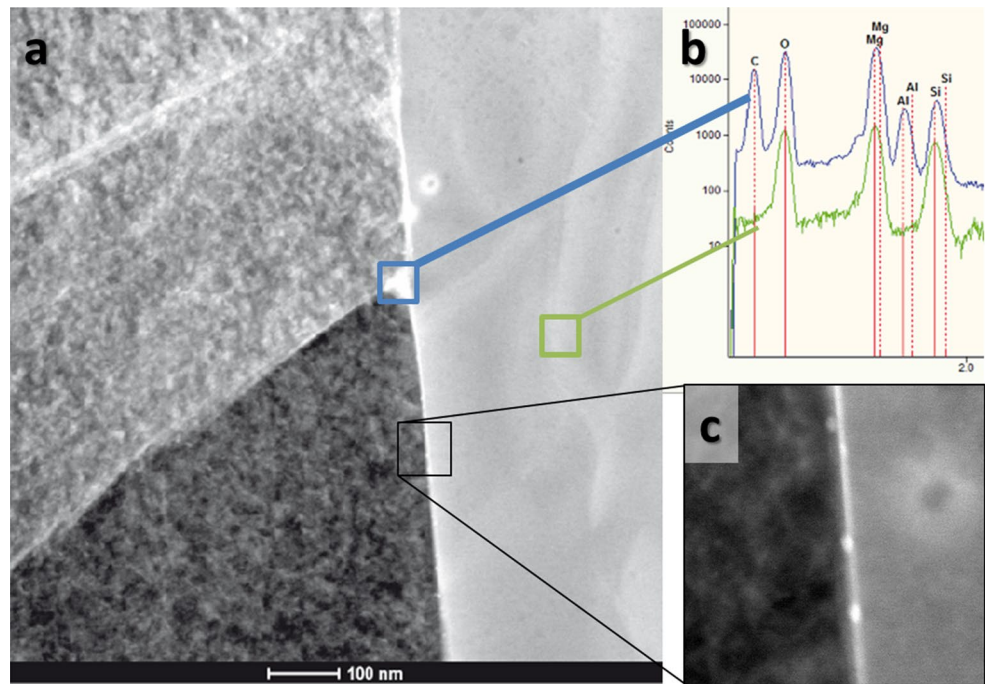
angles (circles in Fig. 2c) as representative for microstructure near equilibrium (Fig. 2a–d). Nevertheless, small angle grain boundaries are present, as also evident from the disorientation distribution function shown in Fig. 2e. Some grain boundaries are sutured (Fig. 2c pink grain, lower middle). Please note that a similar microstructure with similarly wide grain size distribution has been investigated to obtain the GBCD and GBPD in SrTiO3 (Saylor et al. 2004a) and was used to further establish the stereology approach. The calculated random distribution for orthorhombic materials is plotted for comparison. The crystallographic preferred orientation of this sample is weak (Fig. 2f), and might be related to the HIP procedure and initial compaction. The CPO shows a preferred alignment of the c-axis. Figure 1g shows the GBPD, the distribution of grain-boundary areas averaged over all disorientations. In otherwords, each crystal's surface area is displayed as if their crystal lattices were oriented the same. {100} surfaces occur more frequently than {010} and the frequency of {001} is close to a random distribution. The orthorhombic structure is well reflected by three perpendicular diads. The proposed average crystal habit is shown in Fig. 2h using the area ratios of the three principal habit planes (using the concept of Kim and Rohrer 2004). TEM allowed studying the grain boundary structure at the nm-scale, showing that the grain boundaries are straight or slightly curved, but at places include precipitates (Fig. 3a, c). Using energy dispersive X-ray spectroscopy at triple junctions, we detected elevated Al contents compared to the crystal interior as shown in Fig. 3b.

Sample 2 The lherzolite xenolith is composed of forsteritic olivine $(Mg,Fe)_2SiO_4$, with an Mg# between 89.7 and 90.3. Enstatitic pyroxene $(Mg,Fe)_2Si_2O_6$, diopsidic clinopyroxene $Ca(Fe,Mg)Si_2O_6$ and spinel $MgAl_2O_4$. The sample has a porphyroclastic microstructure characterized by mm-scale clasts of olivine and pyroxenes, surrounded by a relatively fine-grained matrix of recrystallized grains of these three phases (Fig. 4a, b). The presence of subgrain walls in the olivine porphyroclasts is ubiquitous, and many have dimensions similar to the recrystallized grains. Due to the presence of subgrains, the total grain boundary area is shifted towards lower disorientation angles in the disorientation distribution (Fig. 4c). The recrystallized olivine grains are predominantly strain free and display triple junctions at 120° angles, suggesting the approaching textural equilibrium. The CPO of this sample is similar to the one of the synthetic forsterite sample. It is characterized by [001] alignment towards the center of the inverse pole figure (Fig. 4d). According to Scott et al. (2014) the equilibration temperature in the studied xenolith is around 950 °C. The GBPD of the natural sample (Fig. 4e) is qualitatively very similar to that of the HIP sample, with both samples displaying maxima at the poles of [100], [010] and [001] planes.

Based on the similarity between the GBPDs derived for sample 1 and 2, we will further evaluate the statistically more significant data set from sample 1 where the CPO is close to random to deduce what are the most frequent grain boundaries by using two different criteria:

Fig. 4 Natural Xenolith from New Zealand. **a** EBSD map for all 4 phases. The crystal orientation is color coded as shown in the *inset*. **b** EBSD map of the same region as in (**a**) and same color code, but here shown are only the forsterite orientations after a pseudo-symmetry correction and a grain dilatation as described in methods. The grain size is variable with an average size of 60 μm and low-angle grain boundaries are frequent. **c** Length fraction of the grain boundary segments versus disorientation angle of the adjacent crystals; the *blue curve* shows the normal distribution for orthorhombic crystal lattices. **d** Orientation distribution function plotted for each crystals [001] direction. Weak CPO is indicated. **e** Grain boundary plane distribution. {100} surfaces occur more frequently than {010} and {001} displays a normal distribution. The general features are similar to those of the HIP sample, but with fewer statistics
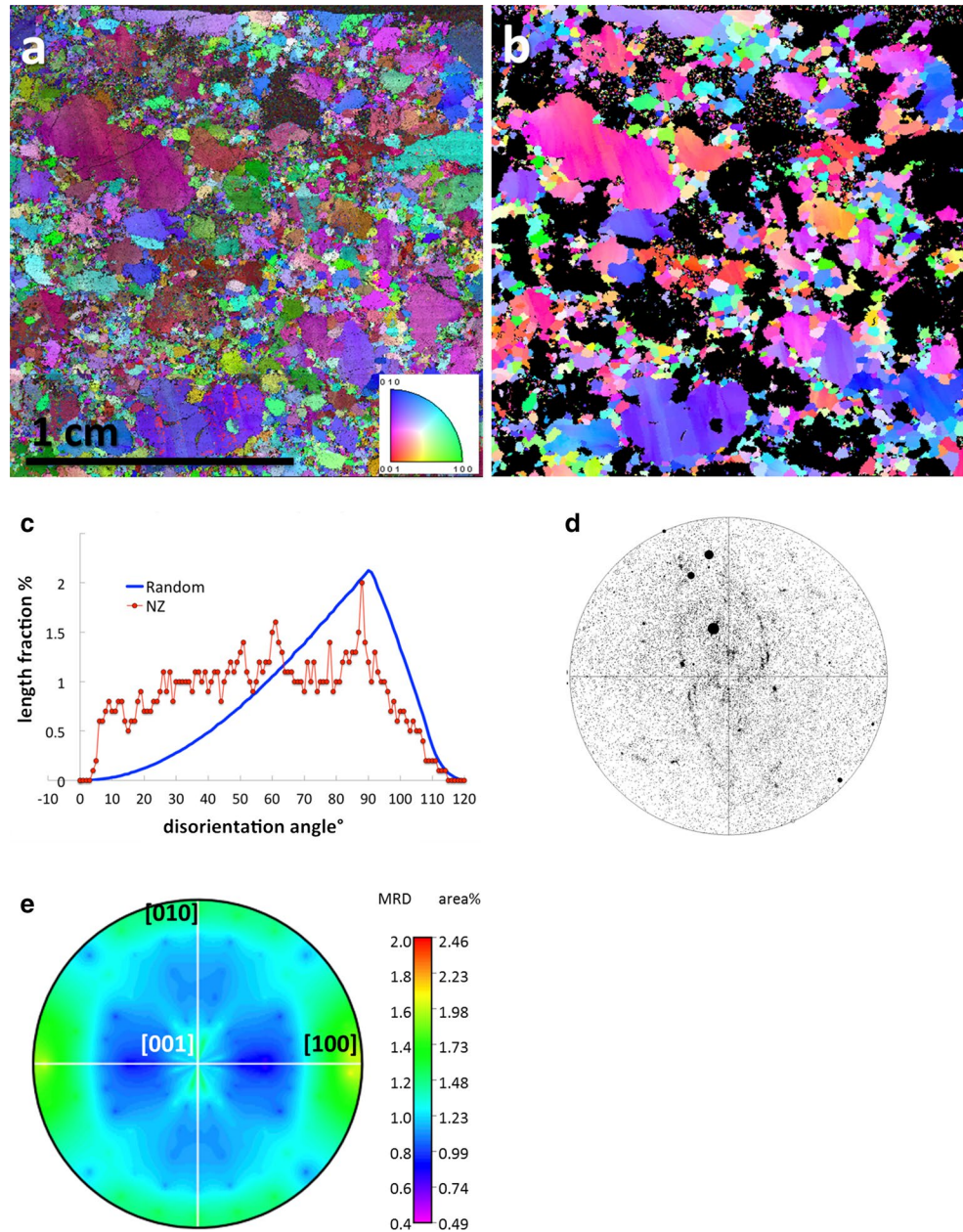
1. We investigated the distribution of grain boundaries in axis-angle space to find the rotation axis connecting two grains with a given disorientation. Figure 5 shows the rotation axis distribution for grain boundaries were the neighboring grains display a defined disorientation, in disorientation intervals of 10°. This is called the axis-angle distribution. The most central observations are: (1) Low angle grain boundaries, defined as 0°–25° grain boundaries in accordance with Heinemann et al. 2005 and Adjaoud et al. (2012), are generally disoriented about the [010] and [001] axis. (2) At 60° disorientation the preferred axis of rotation is the [100] axis. (3) At 90° disorientation the preferred axis of rotation is the [001] axis.

The full five parameter grain boundary analysis is depicted in Fig. 6. Figure 6a shows the disorientation distribution where low-angle disorientations occur with large length fractions. In Fig. 6b the axis distribution for 10° disorientations is repeated from Fig. 5 to illustrate its relation. In Fig. 6c the grain boundary plane distribution for 10° disorientations about [010] is displayed. The plot is dominated by tilt grain boundaries as indicated by their normals being perpendicular to the disorientation axis. Asymmetric low angle tilt grain boundaries are frequent as indicated by the asymmetry of this specific plane distribution.

In Fig. 6d the axis distribution for 60° disorientations is shown, with maximum at the [100]-axis. Figure 6d shows the

Fig. 5 Axis distribution at the indicated disorientation angles. The stereographic projection is done along the [001] direction in all stereograms, indicated only in the axis distribution of 10°. Preferred axis of disorientation show higher MRD values, the color scale is variable and indicated in the *same box* as the respective axis distribution. The low-angle grain boundaries at about 10° and 20° disorientation show a marked preference for misorientations about either {010} or {100} axes. High angle grain boundaries show no preference of being disoriented about specific axes, except at disorientations of 60° and 90°. This gives 60°/[100] and 90°/[001] as the most abundant axes angle pairs that are further evaluated in Fig. 5
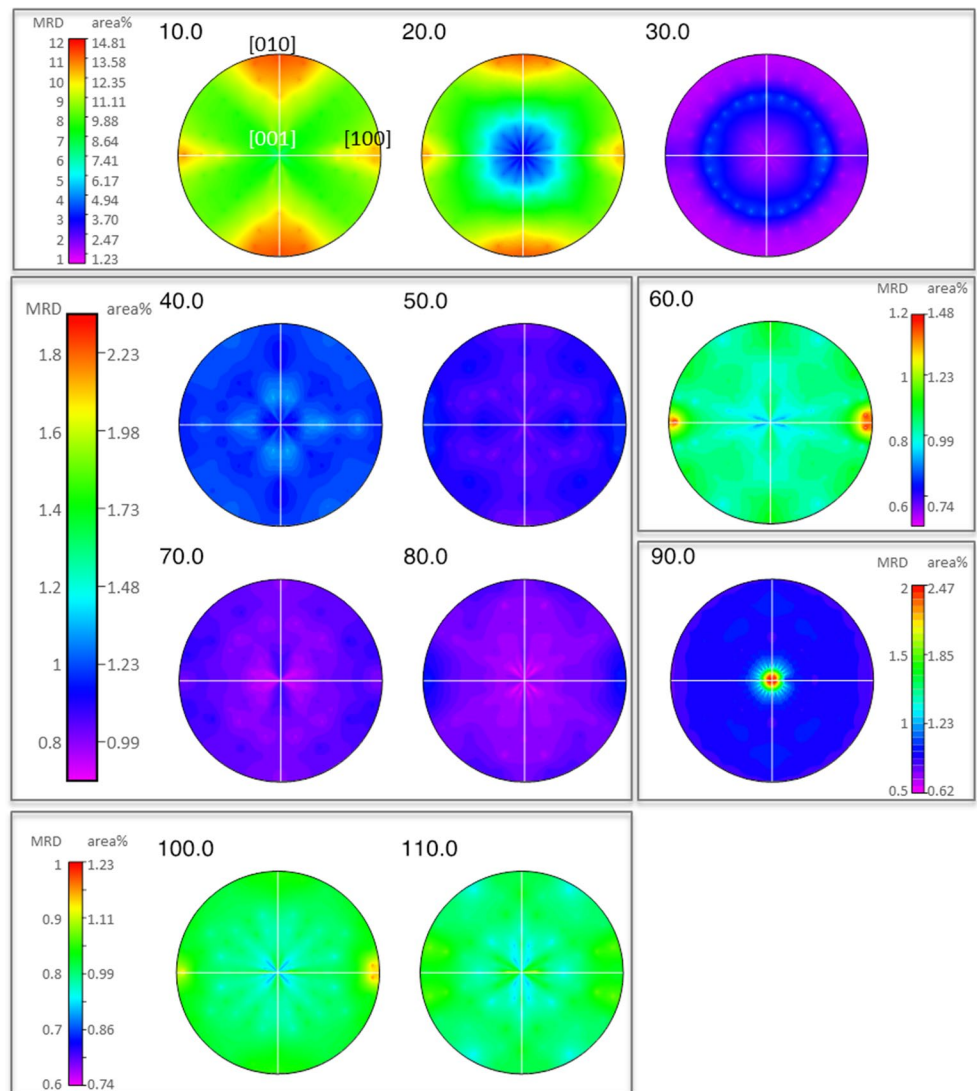
GBPD for grain boundary planes disoriented by 60° about the [100] axis, showing maxima in the [100] zone. This suggests a preference for tilt grain boundaries, eventually that (051);(031);(053);(15 15 16);(212);(0–11) planes seem to be most frequently involved in these grain boundaries.

In Fig. 6f the GBPD for 90°/[001] grain boundaries is displayed. The dominant planes are {100}, {010} and {001} grain boundary plane. The {100}, {010} planes show that there are asymmetric tilt boundaries with a (100) plane on one side of the bicrystal and a (010) plane on the complement, whereas the {001} planes represent 90° twist boundaries about [001] (Fig. 6g). A quantitative evaluation of the distribution shows that about 12 area % of the total grain boundary area is made of 90°/[001] tilt boundaries. This analysis at this particular disorientation, with the 90° disorientation constraint, allows to say that the vast majority (24 area %) of the grain boundaries are (100)∥(010) and (001)∥(001). This following considerations show that also (100)∥(100) is a favorable contact plane.

2. Which are the grain boundary planes that have the highest likelihood of being in direct contact? We evaluated the most frequent planes observed in the GBPD (Fig. 2d), which are the (100) planes. Then we approximated that grain boundary traces in a zone of (100) planes are exactly (100) planes, then the orientation of the complementary grain boundary is completely determined. This procedure yields a very high probability of (100) grain boundaries being in contact with (100) grain boundaries (Fig. 7). Considering the approximation mentioned, the quantitative results in the distribution for the percentage area can only serve as rough guide. However, (100)∥(100) twist grain boundaries have a tendency to be present at all disorientations.
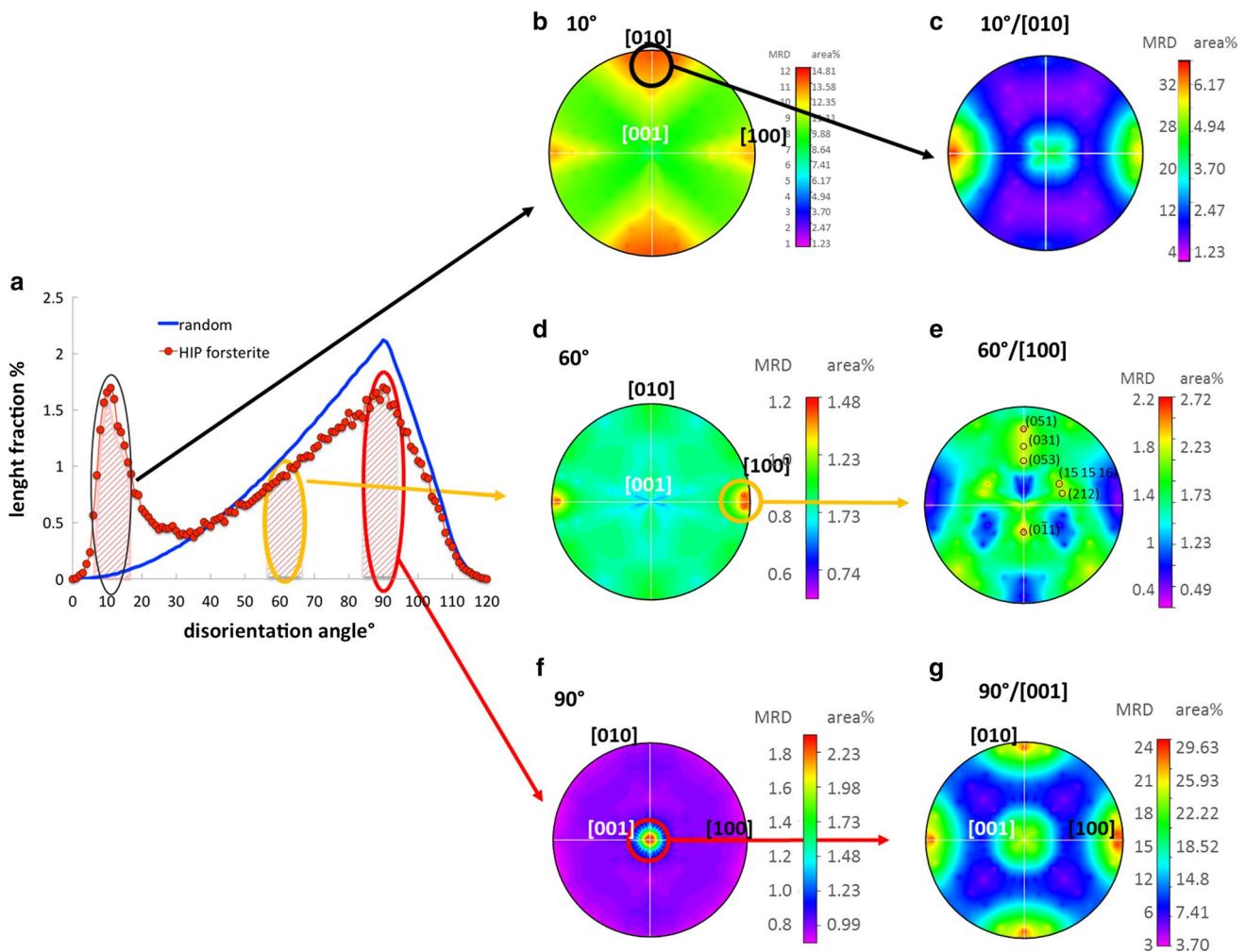
Fig. 6 Illustration of displaying the full GBCD. The disorientation distribution (**a**) is used to gain a first idea of the disorientations relevant to the system investigated. Besides the peak at 90°, typical for all orthorhombic crystal systems, the peak at low-angle grain boundaries is pronounced. Plotting the axis angle distribution (e.g. in this Figure, and Fig. 6b, d, e) for specific disorientations allows identification of frequent disorientation axis. **b** The most important axes of disorientations at 10° disorientation, **c** the GBPD at 10°/[010] is dominated by {100} planes, indicative of tilt grain boundaries. *Note* that the location of high symmetry grain boundary plane normals for pure twist grain boundaries are parallel to the disorientation axis, whereas tilt grain boundaries have plane normal that are perpendicular to the disorientation axis. For any grain boundary plane normals of the two planes that form the grain boundary are separated by disorientation angle (an explanatory scheme is given in Pennock et al. 2009). **d** That high values of MRD are observed for [100] axis at 60° disorientation. The corresponding GBPD (**e**) is dominated by low index planes: from *top* to *bottom*: (051);(031);(053);(15 15 16);(212);(0–11). Tilt boundaries are located along the vertical of the GBPD plot and twist boundaries would appear as a higher MRD region around the [001] axis,

which is not the case. The (0–11) plane belongs to a symmetric tilt grain boundary of 60°/[100] with (011) planes in contact. The (051), (031) and (053) planes are asymmetric tilt grain boundaries. The two remaining planes with higher MRD values are associated with grain boundaries of mixed tilt and twist character. **f** For grains that have 90° disorientations, the [001] axis is the dominant axis of rotation (**g**). A plot of the grain boundary plane distribution for the identified axis and angle reveals that the planes most frequently involved in these grain boundaries are {010} and {100} planes. Quantitative evaluation of 90° disorientations: Integration of the population from 85° to 95° disorientation yields that 17 % by length of the grain boundaries have this disorientation (**a**). The analysis in (**f**) has a discretization of 9 bins per 90° therefore the fraction of grain boundaries evaluated actually ranges from 80° to 100°, with each bin populated by more than 2.23 area %, yielding 29.4 % of the total area. These grain boundaries are almost exclusively disorientated around the c-axis. **g** Due to the mutual 90°/[001] tilt relation between [010] and [100] relation, nearly 12 area % of the total grain boundary area is made of 90°/[001] tilt boundaries. Furthermore, 24 area % are made (100)‖(010) and (001)‖(001) grain boundaries with 90° misorientation

Discussion

The disorientation distribution of the natural and synthetic olivine aggregate is similar to the random disorientation

distribution calculated for orthorhombic crystal systems as shown by Morawiec (2010), with the exception of the low-angle grain boundaries. Initial compaction during experimental synthesis frequently shows the development

Fig. 7 Analysis of the grain boundary contact plane distribution for (001) planes. In **a** the grain boundary plane distribution from Fig. 1d is plotted. In **b** only those grain boundary planes that are in contact with (001) planes are displayed. The interpretation is that (001) planes are preferentially in contact with (001) planes
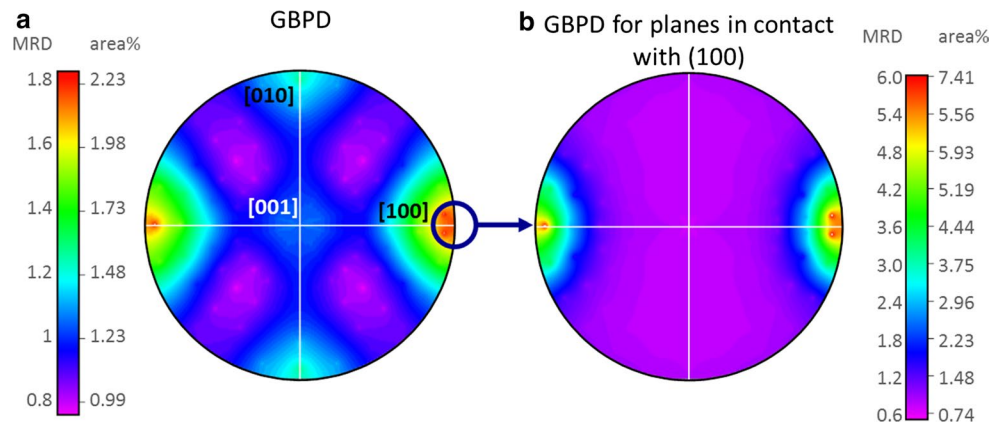
of tilt walls parallel to (100), probably resulting from the dominance of (010)[100] slip system (Nicolas et al. 1973; Wenk et al. 1991; Tommasi et al. 2008; Farla et al. 2011). However, the here observed low angle tilt grain boundaries are aligned parallel (100). The orientation of tilt walls and analyses of the CPO might allow to give more information on the mechanism influencing the microstructure (Friedel 1964; Wenk et al. 1991; Lloyd et al. 1997; Wheeler et al. 2001). Here the low-angle grain boundaries are not further evaluated, as the main focus of the work lies on high-angle grain boundaries.

Both materials show a weak [001] CPO (Figs. 2f, 3d). The CPO may imply former processes including dynamic recrystallization, e.g. subgrain rotation and/or grain boundary migration. The first normally has a minor effect on the microstructure; the latter can even result in a weakening of CPOs. Furthermore, static recrystallization may also result in weak CPOs (Heilbronner and Tullis 2006).

The grain boundary plane distribution reveals that high-angle grain boundaries are terminated by low-index planes. {100} surfaces occur more frequently than {010} and {001} displays the population expected for a random distribution. This anisotropic area distribution is in agreement with similar findings on other materials (e.g. MgO, TiO_2, Al_2O_3) that show a similar preference for low index internal surface planes that produces an anisotropy in the GBPD (Saylor et al. 2004b; Pang and Wynblatt 2006; Dillon and Rohrer 2009; Papillon et al. 2009). The area distribution of the surfaces in polycrystalline forsterite differs significantly from the surface area distribution of an olivine single crystal as calculated for single crystals in contact with *a fluid or melt* (Watson et al. 1997; de Leeuw et al. 2000; Gurmani et al. 2011) or the habits of single crystals grown in a fluid displayed in standard mineralogy books (e.g. Tröger 1967; Deer et al. 1992). These studies agree that the {010} surfaces have the lowest energy, followed by the {100} and the {001} surfaces, respectively. We interpret this difference with respect to our data to be related to the surface (or interface) energy, determined by the relative orientation of

the two crystals, which is different from the surface energy of a crystal in contact with a different phase. This is in agreement with previous conclusions that the grain boundary energy significantly depends on the type of material in contact with the grain boundary (Pang and Wynblatt 2006; Papillon et al. 2009), for example segregated impurities, precipitates or the presence of a melt or fluid.

No preference for special (low Σ CSL) grain boundaries of any type is observed in our samples. This may indicate that grain boundary energy minimization is controlled by surface energy reduction of the individual grains in contact and not by grain boundary energy reduction through adapting the grain boundary plane orientation of special atomic configuration across the interface. Thus it is further evidence that the sigma number of a grain boundary is not correlated with its frequency. The ideal shape or minimum surface energy depends on the material the individual crystal is in contact with, e.g. another crystal, melt, fluid, or segregated elements. However, the observation that our grain boundary segments between triple junctions are not perfectly straight, but slightly curved lines, indicates that jags and facets on the nanometer scale allow energy minimization by breaking the grain boundary planes in a manner to obtain as much area as possible of low-index surfaces that are also the low energy surfaces for each of the individual crystals. This observation is in agreement with the rare observation of twin systems for forsterite dominated olivine. Generally, twinning frequency is related to calcium content (Larsen et al. 1941) and thus twins are reported in basic calcium rich alkali-rocks such as olivine nephelinits (Ankaratite), Melilithbasalts, Polzenite, Venanzite etc., which has been observed as early as 1935 (Conrad 1935). In such Ca-rich olivines twins are observed along {011}, {012} or {031}. These twin laws are generalized for olivines of all compositions (e.g. Tröger 1967; Deer et al. 1992), but the authors of the present contribution are not aware of any reported twin example in Ca-free olivines. Other orthorhombic crystals such as for example aragonite develop well-known (110)-twin (Wooster 1982; McTigue

and Wenk 1985; Massaro et al. 2014). We use our data for the GBPD to construct an average crystal shape (Fig. 1h) by following the procedure outlined in (Kim and Rohrer 2004) and ignoring planes that have <1.5 % of the full grain boundary area. We note that maybe not one crystal in our sample actually has such an ideal shape, because at contacts with neighboring grains the shape is truncated. This analyses yields area ratios between {100}:{010}:{001} planes of 9:6:5. Note that the idealized grain shape is not only relevant in solid–liquid systems, but also in solid–solid systems as the production of gaps is circumvented by faceting and thus a model rock formed of the ideal shape would still show the same surface areas.

Our study indicates no higher probability of grains being disoriented by 60° than predicted from random distributions. However, 60° disorientations tend to rotate about the [100] axis, which is consistent with the pseudo-symmetry relation in olivine due to its hexagonal closed packed oxygen sublattice. As surface energy and GBPD are inversely related, it seems that this specific grain boundary has a significantly lower energy. This hypotheses can be confirmed for the symmetric 60°/[100] (011) grain boundary, where previous numerical simulations find that this specific grain boundary has indeed a lower free energy (Adjaoud et al. 2012). This can also result in specific strain field distributions and thereby affect deformation by grain boundary migration (Cordier et al. 2014). Our observation strengthen the observation of Faul and Fitz Gerald (1999), who found that melt is reluctant to cover 60°[100] grain boundaries, implying that the grain boundary energy is a significant factor for grain boundary wetting, melt segregation and extraction. Wetting changes with grain boundary energy changes are in agreement with a recent modeling study (Ghanbarzadeh et al. 2014). However, if Faul and Fitz Gerald's (1999) finding is true, grain boundaries with a 90° rotation about [001] should resist wetting even more.

Generally, even though our discussion focuses on wetting, the principle of grain boundary energy variation will also effect grain boundary diffusion or deformation at grain boundaries, where grain boundaries of higher frequency, thus lower energy will be harder to deform and have lower diffusivities.

Summary and conclusion

The grain boundary area distribution of olivine shows that low index grain boundary planes occur more frequently compared to random grain boundary planes. The disorientation between the adjacent crystals is consistent with a random distribution, showing that energy minimization is mainly achieved by surface energy minimization of each individual crystal to form grain boundaries with low energy surfaces. Furthermore, energy minimization seems to occur by faceting of the grain boundary planes in a manner to obtain as much area as possible of low-index surfaces that are also the low energy surfaces for individual crystals in contact to a neighboring crystal.

The grain boundary area distribution of polycrystalline olivine therefore resembles the stereographic projection of an idiomorphic single crystal. We conclude, that the most frequent grain boundaries in olivine rocks are 90° tilt grain boundaries about the [001] axis with (100), (010) and (001) planes in contact. The best approximation for a 3D grain boundary network is by building a space filling structure out of our proposed average crystal shape (Fig. 2h).

Finally, we highlight that the GBPD and GBCD are intrinsic material properties (Rohrer 2007, 2011a), and that observed GBPD and GBCD differences in differently produced synthetic and natural rocks will affect the overall grain boundary network properties. Therefore, the GBCD should be carefully evaluated for materials subject to deformation experiments, especially in deformation regimes where grain boundary sliding and grain boundary diffusion are expected. Furthermore the GBCD will affect diffusion rates at low temperatures and thus alteration rates.

References

Adjaoud O, Marquardt K, Jahn S (2012) Atomic structures and energies of grain boundaries in Mg_2SiO_4 forsterite from atomistic modeling. Phys Chem Miner 39:749–760. doi:10.1007/s00269-012-0529-5

Atkinson A, Taylor RI (1979) The diffusion of Ni in the bulk and along dislocations in NiO single crystals. Philos Mag A 39:581–595. doi:10.1080/01418617908239293

Bagdassarov N, Laporte D, Thompson AB (2000) Physics and chemistry of partially molten rocks. Kluwer Academic Publishers, Berlin

Becker JK, Bons PD, Jessell MW (2008) A new front-tracking method to model anisotropic grain and phase boundary motion in rocks. Comput Geosci 34:201–212. doi:10.1016/j.cageo.2007.03.013

Bollmann W (1962) On the analysis of dislocation networks. Philos Mag 7:1513–1533. doi:10.1080/14786436208213290

Bollmann W (1970) Crystal defects and crystalline interfaces. Springer, New York

Brandon DG (1966) The structure of high-angle grain boundaries. Acta Metall 14:1479–1484

Brandon D (2010) 25 Year perspective defining grain boundaries: an historical perspective The development and limitations of coincident site lattice models. Mater Sci Technol 26:762–773. doi:10.1179/026708310X12635619987989

Campbell GH, Plitzko JM, King WE et al (2004) Copper Segregation to the Σ 5 (310)/[001] symmetric tilt grain boundary in aluminum. Interface Sci 12:165–174

Chadwick GA, Smith DA (eds) (1976) Grain boundary structure and properties. Academic Press, London, pp 388. ISBN: 0121662500, 9780121662509

Cmíral M, Fitz Gerald JD, Faul UH, Green DH (1998) A close look at dihedral angles and melt geometry in olivine-basalt aggregates: a TEM study. Contrib Mineral Petrol 130:336–345

Conrad B (1935) Notiz über Zwillinge und Drillinge gesteinsbildender Olivine. Schweizerische Mineral und Petrogr Mitteilungen 15:160–167

Cordier P, Demouchy S, Beausir B et al (2014) Disclinations provide the missing mechanism for deforming olivine-rich rocks in the mantle. Nature. doi:10.1038/nature13043

Dai L, Li H, Hu H, Shan S (2008) Experimental study of grain boundary electrical conductivities of dry synthetic peridotite under high-temperature, high-pressure, and different oxygen fugacity conditions. J Geophys Res 113:B12211. doi:10.1029/2008JB005820

Dai L, Li H, Hu H et al (2013) Electrical conductivity of Alm82Py15Grs3 almandine-rich garnet determined by impedance spectroscopy at high temperatures and high pressures. Tectonophysics 608:1086–1093. doi:10.1016/j.tecto.2013.07.004

De Leeuw NH, Parker SC, Catlow CRA, Price GD (2000) Modelling the effect of water on the surface structure and stability of forsterite. Phys Chem Miner 27:332–341. doi:10.1007/s002690050262

Deer WA, Howie RA, Zussman J (1992) An introduction to the rock forming minerals, 2nd edn. Prentice Hall, Englewood Cliffs

Dillon SJ, Rohrer GS (2009) Mechanism for the development of anisotropic grain boundary character distributions during normal grain growth. Acta Mater 57:1–7. doi:10.1016/j.actamat.2008.08.062

Farla RJM, Gerald JDF, Kokkonen H et al (2011) Slip-system and EBSD analysis on compressively deformed fine-grained polycrystalline olivine. Geol Soc Lond Spec Publ 360:225–235. doi:10.1144/SP360.13

Farver J, Yund R (2000) Silicon diffusion in forsterite aggregates: implications for diffusion accommodated creep. Geophys Res Lett 27:2337–2340

Farver JR, Yund A, Rubie C (1994) Magnesium grain boundary diffusion in forsterite aggregates at 1000°–1300°C and 0.1 MPa to 10 GPa. J Geophys Res 99(94):19809–19819

Faul UH (2001) Melt retention and segregation beneath mid-ocean ridges. Nature 410:920–923. doi:10.1038/35073556

Faul UH, Fitz Gerald JD (1999) Grain misorientations in partially molten olivine aggregates: an electron backscatter diffraction study. Phys Chem Miner 26:187–197. doi:10.1007/s002690050176

Faul UH, Fitz Gerald JD, Jackson I (2004) Shear wave attenuation and dispersion in melt-bearing olivine polycrystals: 2. Microstructural interpretation and seismological implications. J Geophys Res 109:202. doi:10.1029/2003JB002407

Fitz Gerald JD, Parsons I, Cayzer N (2006) Nanotunnels and pullaparts: defects of exsolution lamellae in alkali feldspars. Am Mineral 91:772–783. doi:10.2138/am.2006.2029

Fliervoet TF, Drury MR, Chopra PN (1999) Crystallographic preferred orientations and misorientations in some olivine rocks deformed by diffusion or dislocation creep. Tectonophysics 303:1–27. doi:10.1016/S0040-1951(98)00250-9

Frank F (1951) The resultant content of dislocations in an arbitrary intercrystalline boundary. Rep. a Symp. Plast. Deform. Cryst. solids. Carnegie Inst. Technol

Friedel J (1964) Deslocations in crystals. Addison-Wesley Publishing Company, Pergamon Press, Reading

Garapic G, Faul UH, Brisson E (2013) High-resolution imaging of the melt distribution in partially molten upper mantle rocks: evidence for wetted two-grain boundaries. Geochem Geophys Geosyst 14:1–11. doi:10.1029/2012GC004547

Gardés E, Wunder B, Marquardt K, Heinrich W (2012) The effect of water on intergranular mass transport: new insights from diffusion-controlled reaction rims in the MgO–SiO$_2$ system. Contrib Mineral Petrol 164:1–16. doi:10.1007/s00410-012-0721-0

Ghanbarzadeh S, Prodanović M, Hesse MA (2014) Percolation and grain boundary wetting in anisotropic texturally equilibrated pore networks. Phys Rev Lett 113:048001. doi:10.1103/PhysRevLett.113.048001

Ghosh DB, Karki BB (2014) First principles simulations of the stability and structure of grain boundaries in Mg$_2$SiO$_4$ forsterite. Phys Chem Miner 41:163–171. doi:10.1007/s00269-013-0633-1

Gleiter H, Chalmers B (1972) High-angle grain boundaries. Pergamon Press, Oxford

Grimmer H (1989) Coincidence orientations of grains in rhombohedral materials. Acta Crystallogr Sect A Found Crystallogr 45:505–523. doi:10.1107/S0108767389002291

Gurmani SF, Jahn S, Brasse H, Schilling FR (2011) Atomic scale view on partially molten rocks: molecular dynamics simulations of melt-wetted olivine grain boundaries. J Geophys Res 116:B12209. doi:10.1029/2011JB008519

Hammond WC, Humphreys ED (2000) Upper mantle seismic wave attenuation: effects of realistic partial melt distribution. J Geophys Res 105:10987. doi:10.1029/2000JB900042

Hartmann K, Wirth R, Markl G (2008) P-T-X-controlled element transport through granulite-facies ternary feldspar from Lofoten, Norway. Contrib Mineral Petrol 156:359–375

Hartmann K, Wirth R, Heinrich W (2010) Synthetic near Σ5 (210)/[100] grain boundary in YAG fabricated by direct bonding: structure and stability. Phys Chem Miner 37:291–300. doi:10.1007/s00269-009-0333-z

Hayden LA, Watson EB (2008) Grain boundary mobility of carbon in earth's mantle: a possible carbon flux from the core. Proc Natl Acad Sci USA 105:8537–8541. doi:10.1073/pnas.0710806105

Heilbronner R, Tullis J (2006) Evolution of c axis pole figures and grain size during dynamic recrystallization: results from experimentally sheared quartzite. J Geophys Res Solid Earth 111:1–19. doi:10.1029/2005JB004194

Heinemann S, Wirth R, Gottschalk M, Dresen G (2005) Synthetic [100] tilt grain boundaries in forsterite: 9.9 to 21.5°. Phys Chem Miner 32:229–240. doi:10.1007/s00269-005-0448-9

Hiraga T, Kohlstedt DL (2007) Equilibrium interface segregation in the diopside-forsterite system I: analytical techniques, thermodynamics, and segregation characteristics. Geochim Cosmochim Acta 71:1266–1280. doi:10.1016/j.gca.2006.11.019

Hiraga T, Anderson IM, Kohlstedt DL et al (2003) Chemistry of grain boundaries in mantle rocks. Am Miner 88:1015–1019. doi:10.1038/nature02259

Hiraga T, Hirschmann MM, Kohlstedt DL (2007) Equilibrium interface segregation in the diopside-forsterite system II: applications of interface enrichment to mantle geochemistry. Geochim Cosmochim Acta 71:1281–1289

Hirth G, Kohlstedt DL (1995) Experimental constraints on the dynamics of the partially molten upper mantle: deformation in the diffusion creep regime. J Geophys Res 100:1981–2001. doi:10.1029/94JB02128

Jackson I (2004) Shear wave attenuation and dispersion in melt-bearing olivine polycrystals: 1. Specimen fabrication and mechanical testing. J Geophys Res 109:B06201. doi:10.1029/2003JB002406

Kaur I, Mishin Y, Gust W (1995) Fundamentals of grain and interphase boundary diffusion, 3rd edn. Wiley, Chichester

Keller LM, Götze LC, Rybacki E, Dresen G, Abart R (2010) Enhancement of solid-state reaction rates by non-hydrostatic stress effects on polycrystalline diffusion kinetics. Am Miner 95:1399–1407. doi:10.2138/am.2010.3372

Khorashadizadeh A, Raabe D, Zaefferer S et al (2011) Five-parameter grain boundary analysis by 3D EBSD of an ultra fine grained CuZr alloy processed by equal channel angular pressing. Adv Eng Mater 13:237–244. doi:10.1002/adem.201000259

Kim C-S, Rohrer GS (2004) Geometric and crystallographic characterization of WC surfaces and grain boundaries in WC-Co composites. Interface Sci 12:19–27. doi:10.1023/B:INTS.0000012291.81411.dc

Kim CS, Hu Y, Rohrer GS, Randle V (2005) Five-parameter grain boundary distribution in grain boundary engineered brass. Scr Mater 52:633–637. doi:10.1016/j.scriptamat.2004.11.025

King AH, Singh A (1994) The coincidence site lattice model to non-cubic materials. J Phys Chem Solids 55:1023–1033

Kruhl JH, Wirth R, Morales LFG (2013) Quartz grain boundaries as fluid pathways in metamorphic rocks. J Geophys Res Solid Earth 118:1957–1967. doi:10.1002/jgrb.50099

Larsen ES, Hurlbut CS, Buie BF, Burgess CH (1941) Igneous rocks of the Highwood Mountains, Montana. Bull Geol Soc Am 52:1841–1856

Le Claire AD (1963) The analysis of grain boundary diffusion measurements. Br J Appl Phys 14:351–356

Li J, Dillon SJ, Rohrer GS (2009) Relative grain boundary area and energy distributions in nickel. Acta Mater 57:4304–4311

Lloyd GE, Farmer AB, Mainprice D (1997) Misorientation analysis and the formation and orientation of subgrain and grain boundaries. Tectonophysics 279:55–78. doi:10.1016/S0040-1951(97)00115-7

Marquardt K (2011) Bicrystals to study grain boundary diffusion: special versus random grain boundaries. In: Geophysical research abstracts, vol 13, abstr 6790

Marquardt K, Petrishcheva E, Gardés E et al (2011) Grain boundary and volume diffusion experiments in yttrium aluminium garnet bicrystals at 1723K: a miniaturized study. Contrib Mineral Petrol 162:739–749. doi:10.1007/s00410-011-0622-7

Massaro FR, Bruno M, Rubbo M (2014) Surface structure, morphology and (110) twin of aragonite. CrystEngComm 16:627. doi:10.1039/c3ce41654b

McLean D (1957) Grain boundaries in metals. Oxford Clarendon Press, Oxford

McTigue JW, McTigue J, Wenk H-R (1985) Microstructures and orientation relationships in the dry-state aragonit-calcite and calcit-lime phase transformations. Am Mineral 70:1253–1261

Milke R, Wiedenbeck M, Heinrich W (2001) Grain boundary diffusion of Si, Mg, and O in enstatite reaction rims; a SIMS study using isotopically doped reactants. Contrib Mineral Petrol 142:15–26

Morawiec A (1998) Proceedings of the third international conference on grain growth. In: Weiland H, Adams BL, Rollet AD (eds) Proceedings of the third international conference on grain growth, TMS, Warrendale, p 509

Morawiec A (2010) Orientations and rotations computations in crystallographic textures. Springer, Berlin

Nicolas A, Boudier F, Boullier AM (1973) Mechanisms of flow in naturally and experimentally deformed peridotites. Am J Sci 273:853–876. doi:10.2475/ajs.273.10.853

Pang Y, Wynblatt P (2006) Effects of Nb doping and segregation on the grain boundary plane distribution in TiO_2. J Am Ceram Soc 89:666–671. doi:10.1111/j.1551-2916.2005.00759.x

Papillon F, Rohrer GS, Wynblatt P (2009) Effect of Segregating impurities on the grain-boundary character distribution of magnesium oxide. J Am Ceram Soc 92:3044–3051. doi:10.1111/j.1551-2916.2009.03327.x

Pennock G, Coleman M, Drury M, Randle V (2009) Grain boundary plane populations in minerals: the example of wet NaCl after low strain deformation. Contrib Mineral Petrol 158:53–67. doi:10.1007/s00410-008-0370-5

Peters MI, Reimanis IE (2003) Grain boundary grooving studies of yttrium aluminum garnet (YAG) bicrystals. J Am Ceram Soc 72:2002–2004

Poirier JP (1975) On the slip systems of olivine. J Geophys Res 80:4059–4061

Pond RC, Bollmann W (1979) The symmetry and interfacial structure of bicrystals. Philos Trans R Soc Lond Ser A Math Phys Sci 292:449–472

Pond RC, Vlachavas DS (1983) Bicrystallography. Proc R Soc Lond A Math Phys Sci 386:95–143

Randle V (2002) The coincidence site lattice and the "sigma enigma". Mater Charact 47:411–416

Randle V, Davies H (2001) A comparison between three-dimensional and two-dimensional grain boundary plane analysis. Ultramicroscopy 90:153–162

Randle V, Rohrer GSS, Hu Y (2008) Five-parameter grain boundary analysis of a titanium alloy before and after low-temperature annealing. Scr Mater 58:183–186. doi:10.1016/j.scriptamat.2007.09.044

Rohrer GS (2007) The distribution of grain boundary planes in polycrystals. JOM J Miner Met Mater Soc 59:38–42

Rohrer GS (2011a) Grain boundary energy anisotropy: a review. J Mater Sci 46:5881–5895. doi:10.1007/s10853-011-5677-3

Rohrer GS (2011b) Measuring and interpreting the structure of grain-boundary networks. J Am Ceram Soc 94:633–646. doi:10.1111/j.1551-2916.2011.04384.x

Rohrer GS, El-Dasher BS, Miller HM et al (2004a) Distribution of grain boundary planes at coincident site lattice misorientations. Mat Res Soc Symp Proc. doi:10.1557/PROC-819-N7.2

Rohrer GS, Saylor DM, El Dasher B, Adams BL, Rollett AD, Wynblatt P (2004b) The distribution of internal interfaces in polycrystals. Zeitschrift Für Metallkunde 95(4):197–214. doi:10.3139/146.017934

Saylor DM, Rohrer GS (2002) Determining crystal habits from observations of planar sections. J Am Ceram Soc 804:2799–2804

Saylor DM, Morawiec A, Rohrer GS (2002) Distribution and energies of grain boundaries in magnesia as a function of five degrees of freedom. J Am Ceram Soc 85:3081–3083. doi:10.1111/j.1151-2916.2002.tb00583.x

Saylor DM, Morawiec A, Rohrer GS (2003a) Distribution of grain boundaries in magnesia as a function of five macroscopic parameters. Acta Mater 51:3675–3686. doi:10.1016/s1359-6454(03)00181-2

Saylor DM, Morawiec A, Rohrer GS (2003b) The relative free energies of grain boundaries in magnesia as a function of five macroscopic parameters. Acta Mater 51:3675–3686. doi:10.1016/S1359-6454(03)00182-4

Saylor DM, Dasher B, Sano T, Rohrer GS (2004a) Distribution of grain boundaries in $SrTiO_3$ as a function of five macroscopic parameters. J Am Ceram Soc 87:670–676

Saylor DM, El Dasher BS, Rollett AD, Rohrer GS (2004b) Distribution of grain boundaries in aluminum as a function of five macroscopic parameters. Acta Mater 52:3649–3655

Saylor DM, El-dasher BS, Adams BL, Rohrer GS (2004c) Measuring the five-parameter grain-boundary distribution from

observations of planar sections. Metall Mater Trans A 35:1981–1989

Schmeling H, Kruse JP, Richard G (2012) Effective shear and bulk viscosity of partially molten rock based on elastic moduli theory of a fluid filled poroelastic medium. Geophys J Int 190:1571–1578. doi:10.1111/j.1365-246X.2012.05596.x

Schwarz SM, Kempshall BW, Giannuzzi LA, Stevie FA (2002) Utilizing the SIMS technique in the study of grain boundary diffusion along twist grain boundaries in the Cu(Ni) system. Acta Mater 50:5079–5084

Scott JM, Waight TE, van der Meer PHA et al (2014) Metasomatized ancient lithospheric mantle beneath the young Zealandia microcontinent and its role in HIMU-like intraplate magmatism. Geochem Geophys Geosyst. doi:10.1002/2014GC005300

Smith CS (1948) Grains, phases, and interfaces: an interpretation of microstructure. Trans AIME 175(5):15–51. doi:10.1007/s11661-010-0215-5

Sobolev SV, Zeyen H, Stoll G et al (1996) Upper mantle temperatures from teleseismic tomography of French Massif Central including effects of composition, mineral reactions, anharmonicity, anelasticity and partial melt. Earth Planet Sci Lett 139:147–163. doi:10.1016/0012-821X(95)00238-8

Sutton AP, Balluffi RW (1995) Interfaces in crystalline materials. Clarendon Press, Wotton-under-Edge

Suzuki K (1987) Grain-boundary enrichment of incompatible elements in some mantle peridotites. Chem Geol 63:319–334. doi:10.1016/0009-2541(87)90169-0

Takei Y (1998) Constitutive mechanical relations of solid-liquid composites in terms of grain boundary contiguity. J Geophys Res 103:18183–18203

Takei Y, Holtzman BK (2009) Viscous constitutive relations of solid-liquid composites in terms of grain boundary contiguity: 1. Grain boundary diffusion control model. J Geophys Res Solid Earth 114:1–19. doi:10.1029/2008JB005850

Tommasi A, Vauchez A, Ionov DA (2008) Deformation, static recrystallization, and reactive melt transport in shallow subcontinental mantle xenoliths (Tok Cenozoic volcanic field, SE Siberia). Earth Planet Sci Lett 272:65–77. doi:10.1016/j.epsl.2008.04.020

Tommasi A, Knoll M, Vauchez A et al (2009) Structural reactivation in plate tectonics controlled by olivine crystal anisotropy. Nat Geosci 2:423–427. doi:10.1038/ngeo528

Toomey DR, Wilcock WSD, Conder JA et al (2002) Asymmetric mantle dynamics in the MELT region of the East Pacific Rise. Earth Planet Sci Lett 200:287–295. doi:10.1016/S0012-821X(02)00655-6

Tröger WE (1967) Optische Bestimmung der gesteinsbildenden Minerale, Stuttgart

Vauchez A, Tommasi A, Mainprice D (2012) Faults (shear zones) in the earth's mantle. Tectonophysics 558–559:1–27. doi:10.1016/j.tecto.2012.06.006

Villagomez DR, Toomey DR, Geist DJ et al (2014) Mantle flow and multistage melting beneath the Galapagos hotspot revealed by seismic imaging. Nat Geosci 7:151–156

Von Bargen N, Waff HS (1986) Permeabilities, interfacial areas and curvatures of partially molten systems: results of numerical computations of equilibrium microstructures. J Geophys Res Solid Earth 91:9261–9276. doi:10.1029/JB091iB09p09261

Vonlanthen P, Grobety B (2008) CSL grain boundary distribution in alumina and zirconia ceramics. Ceram Int 34:1459–1472

Walte NP, Bons PD, Koehn D (2003) Disequilibrium melt distribution during static recrystallization. Tectonophysics 31:1009–1012

Walte NP, Bons PD, Passchier CW (2005) Deformation of melt-bearing systems—insight from in situ grain-scale analogue experiments. J Struct Geol 27:1666–1679. doi:10.1016/j.jsg.2005.05.006

Wark DA, Watson EB (1998) Grain-scale permeabilities of texturally equilibrated, monomineralic rocks. Earth Planet Sci Lett 164:591–605

Wark DA, Williams CA, Watosn BE, Price JD (2003) Reassessment of pore shapes in microstructurally equilibrated rocks, with implications for permeability of the upper mantle. J Geophys Res 108:2050. doi:10.1029/2001JB001575

Watanabe T (2011) Grain boundary engineering: historical perspective and future prospects. J Mater Sci 46:4095–4115. doi:10.1007/s10853-011-5393-z

Watson GW, Oliver PM, Parker SC (1997) Computer simulation of the structure and stability of forsterite surfaces. Phys Chem Miner 25:70–78. doi:10.1007/s002690050088

Weins M, Chalmers B, Gleiter H, Ashby M (1969) Structure of high angle grain boundaries. Scr Metall 3:601–603

Wenk H-R, Bennett K, Canova GR, Molinari A (1991) Modelling plastic deformation of peridotite with the self-consistent theory. J Geophys Res 96:8337. doi:10.1029/91JB00117

Wheeler J, Prior DJ, Jiang Z et al (2001) The petrological significance of misorientations between grains. Contrib Mineral Petrol 141:109–124. doi:10.1007/s004100000225

Wirth R (1996) Thin amorphous films (1–2 nm) at olivine grain boundaries in mantle xenoliths from San Carlos, Arizona. Contrib Mineral Petrol 124:44–54

Wirth R (2004) Focused Ion Beam (FIB): a novel technology for advanced application of micro- and nanoanalysis in geosciences and applied mineralogy. Eur J Mineral 16:863–876. doi:10.1127/0935-1221/2004/0016-0863

Wooster WA (1982) Atomic arrangements on the twin boundaries of crystals of calcite and aragonite. Mineral Mag 46:265–268

Worden RH, Walker FDL, Parsons I, Brown WL (1990) Development of microporosity, diffusion channels and deuteric coarsening in perthitic alkali feldspar. Contrib Mineral Petrol 104:507–515

Yund RA (1997) Rates of grain boundary diffusion through enstatite and forsterite reaction rims. Contrib Mineral Petrol V126:224–236